THE ASTROPHYSICAL JOURNAL, 915:64 (8pp), 2021 July 1 https://doi.org/10.3847/1538-4357/ac02ce

Low-frequency Waves Upstream of Quasi-parallel Shocks: Two-dimensional Hybrid Simulations

Yufei Hao[1,2,3], Quanming Lu[2,3], Dejin Wu[1], San Lu[2,3], Liang Xiang[1,4], and Yangguang Ke[2,3]
[1] Key Laboratory of Planetary Sciences, Purple Mountain Observatory, Chinese Academy of Sciences, Nanjing, People's Republic of China
[2] CAS Key Laboratory of Geospace Environment, School of Earth and Space Sciences, University of Science and Technology of China, Hefei, People's Republic of China; qmlu@ustc.edu.cn
[3] CAS Center for Excellence in Comparative Planetology, Hefei, People's Republic of China
[4] Key Laboratory of Low Dimensional Quantum Structures and Quantum Control, School of Physics and Electronics, Hunan Normal University, 410081, Changsha, People's Republic of China
Received 2021 March 5; revised 2021 May 16; accepted 2021 May 17; published 2021 July 7

Abstract

In this paper, we study low-frequency waves upstream of quasi-parallel shocks by using two-dimensional (2D) hybrid simulations. Simulation results show that reflected particles can backstream and form a superthermal particle component in plasmas in an area just before the shock front. The component interacts with the incident particles and can result in quasi-parallel and quasi-perpendicular fast magnetosonic waves with comparable wave amplitudes, and they have right-hand and linear polarization, respectively. Further upstream, after being scattered by these upstream waves, the backstreaming particles develop a shell-like velocity distribution so that similar waves can be driven by the free energy from this newly formed distribution, and in this area the quasi-perpendicular waves are dominant over the quasi-parallel ones. Linear theory confirms the generation of these two types of upstream waves.

Unified Astronomy Thesaurus concepts: Interplanetary shocks (829); Shocks (2086); Planetary bow shocks (1246)

1. Introduction

Collisionless shocks are universal and thought to be important because they play a crucial role in the generation of power-law spectra of energetic ions in space and astrophysical environments (Axford et al. 1977; Bell 1978; Blandford & Ostriker 1978; Webb et al. 1995). For a quasi-perpendicular shock, whose shock angle θ_{Bn} (defined as the angle between the shock normal and the upstream magnetic field) is larger than 45°, incident particles can be partially reflected by the shock front and gyrate in the shock foot. Some of these gyrating particles can stay near the shock front for a period of time, which allows them to be accelerated to high energies through shock drift acceleration and shock surfing acceleration (Zank et al. 1996; Lembege et al. 2004; Lu et al. 2009; Yang et al. 2009a, 2009b; Giacalone & Decker 2010; Guo & Giacalone 2010, 2013; Gedalin 2016a, 2016b). All of these reflected particles may not go further upstream and result in a foreshock region as in a quasi-parallel shock, where the upstream background magnetic field always has a larger component in the direction parallel to the shock normal due to its smaller shock angle ($\theta_{\mathrm{Bn}} < 45°$). Additionally, part of the reflected particles can reasonably backstream very far away from the shock front in the upstream region (Burgess 1989; Scholer & Burgess 1992; Lin 2003; Eastwood et al. 2005a, 2005b; Wilson et al. 2013; Liu et al. 2015, 2021; Hao et al. 2016a; Wilson 2016; Lu et al. 2020).

These backstreaming particles will interact with the incident ions upstream of a quasi-parallel shock, which leads to the excitation of ultra-low-frequency (ULF) waves propagating nearly in the direction of the background magnetic field by the resonant electromagnetic ion beam instability (Quest 1988). These waves can then be convected back by incident flow and further interact with newly backstreaming particles when they approach the shock front. This interaction results in their steepening, nonlinear evolution and even refraction of wavevectors near the shock front (Giacalone et al. 1992; Scholer 1993; Scholer et al. 1993; Su et al. 2012a; Wilson 2016). Recently, Blanco-Cano et al. (2006, 2009, 2011) and Omidi (2007) performed 2D global hybrid simulations to investigate the foreshock waves before a bow shock. They suggest that besides the well-known ULF waves excited further upstream, another types of wave mode appears close to the shock front. They are highly oblique fast magnetosonic waves, which are thought to be driven by the ring beam distributions from the shock front rather than generated by the nonlinear evolution of ULF waves. Therefore, the components of upstream waves at a quasi-parallel shock remains controversial. In this paper, we perform 2D hybrid simulations of a plane quasi-parallel shock front with a fixed global shock normal to investigate the waves upstream of quasi-parallel shocks.

2. Simulation Model

In this paper, a 2D hybrid simulation model is employed to study the waves upstream of a quasi-parallel shock. Hybrid simulations frequently treat ions as macroparticles, while electrons are regarded as massless fluid. The plasma has electron and proton components, and charge neutrality is assumed. In the $x - y$ simulation plane, an incident flow with the background magnetic field B_0 moves continuously from left to right and is reflected by the right rigid boundary. The shock is launched by the interaction between the incident flow and the reflected plasma, and the shock propagates toward the left. The periodic boundary condition is used in the y direction. In this simulation, shock angle is $\theta_{\mathrm{Bn}} = 30°$. The incident flow has a fixed bulk velocity $V_{\mathrm{inj}} = 4.5V_{\mathrm{A}}$ (where V_{A} is the Alfvén speed under upstream parameters) and plasma beta $\beta_p = \beta_e = 0.4$ (where p and e denote proton and electron, respectively), and the propagating velocity of this shock front is about $1.0V_{\mathrm{A}}$, so its Alfvén Mach number is about 5.5. The simulation domain

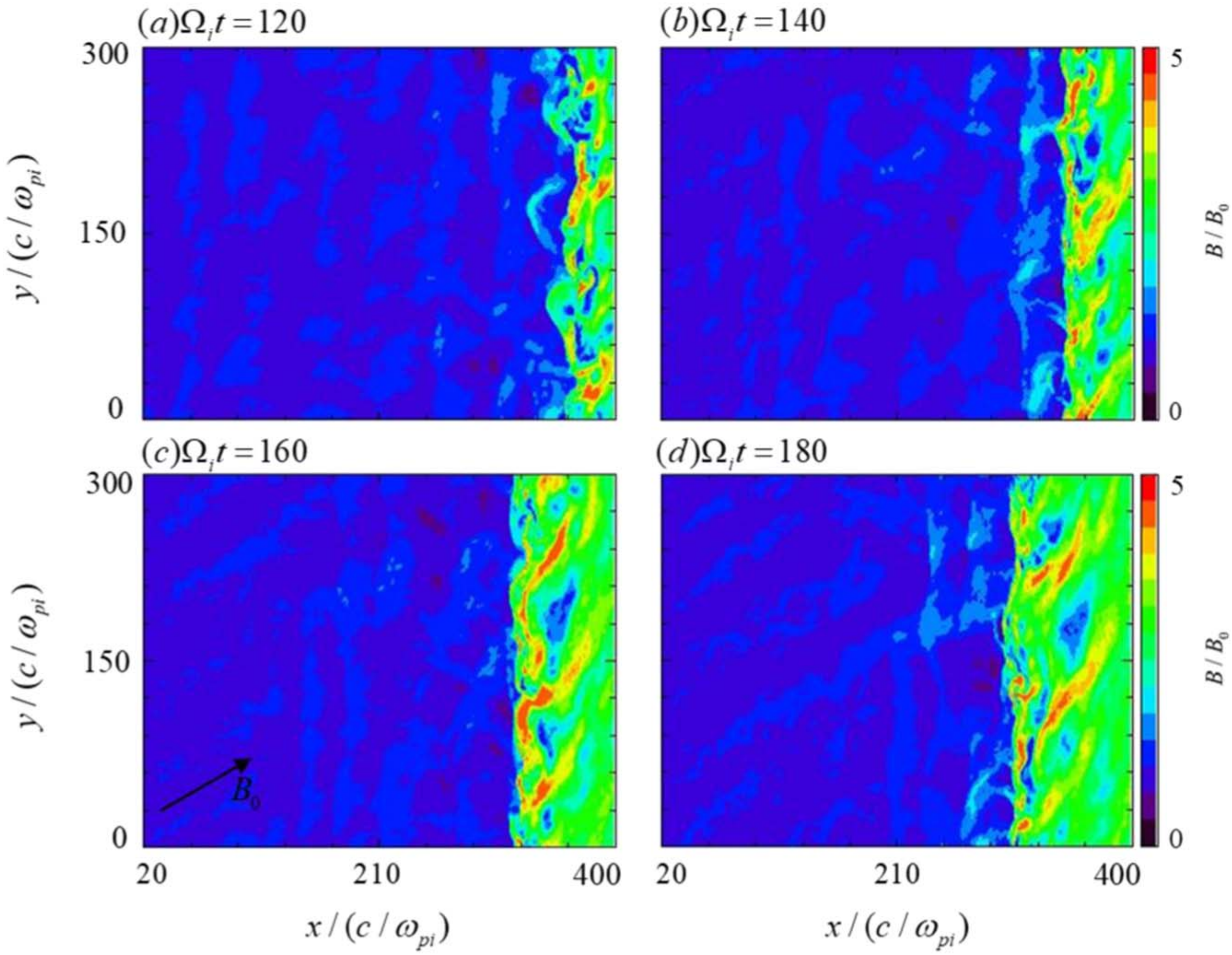

Figure 1. Contour plots of the total magnetic field at times $\Omega_i t$ = (a) 120, (b) 140, (c) 160, and (d) 180. The black arrow indicates upstream background magnetic field B_0.

covers an area of $n_x \times n_y = 1000 \times 300$ grid cells, and the sizes of each grid cell are $\Delta x = 0.5c/\omega_{pi}$ and $\Delta y = 1.0c/\omega_{pi}$ (where c is the light speed and ω_{pi} is the upstream ion plasma frequency). There are 30 macroparticles in each grid cell when they are initially injected. That electron resistivity length expressed as $L_\eta = \eta c^2/(4\pi V_A)$ (where η indicates the interaction of particles with high-frequency waves) is set to be 0.1, and the time step is $\Omega_i t = 0.02$, where Ω_i is the ion gyrofrequency.

3. Simulation Results

In Figure 1, total magnetic fields at $\Omega_i t$ = (a) 120, (b) 140, (c) 160, and (d) 180 are plotted in the simulation plane. In downstream areas, large-scale filamentary magnetic structures can be seen, and they extend over 100 ion inertial lengths from the shock front to further downstream (Hao et al. 2017). The rippled shock front at $\Omega_i t = 120$ evolves into a relative plane one at $\Omega_i t = 140$ due to its merging with new shock fronts shown in Figure 1(a). Meanwhile, ULF waves permeate the upstream area as shown in every panel of Figure 1. However, further upstream in Figures 1(b)–(d), wave fronts seem to be parallel to the upstream background magnetic fields, which means that quasi-perpendicular waves are possibly excited in the region far away from the shock front. While, as suggested by previous simulation results (Scholer & Burgess 1992; Scholer 1993), upstream waves should be quasi-parallel propagating fast magnetosonic waves.

To investigate the properties of these upstream waves, in Figure 2, (a) variations of total magnetic fields $\delta B = B_t - \bar{B}_t$ and (b) particle number density fluctuations $\delta N = N_i - \bar{N}_i$ are displayed in an upstream region ($20c/\omega_{pi} < x < 300c/\omega_{pi}$, $0 < y < 300c/\omega_{pi}$) at $\Omega_i t = 160$, where B_i, N_i, $\bar{B}_i$, and $\bar{N}_i$ denote total magnetic field, particle number density, and their mean values along the y direction, respectively. In Figure 2(a), we can see that the distinct wave fronts are nearly parallel to the upstream background magnetic fields, and some wave fronts close to the shock front seem to be perpendicular to the global shock normal in the x direction. Through particle number density fluctuations, the corresponding wave fronts can be easily identified in Figure 2(b), which suggests that there are indeed some quasi-perpendicular propagating waves and they may be compressive. Wave fronts perpendicular to the x direction are consistent with previous work (Scholer 1993) that suggests refraction of the wavevector of the upstream waves via their interaction with backstreaming particles.

In Figure 3, we plot the variations of total magnetic field and particle number density along three cuts: (a) $y = 50c/\omega_{pi}$, (b) $y = 150c/\omega_{pi}$, and (c) $y = 250c/\omega_{pi}$. Their correlation coefficient is also calculated in the region as shown in Figure 2 and illustrated in the bottom panel. From their variations in

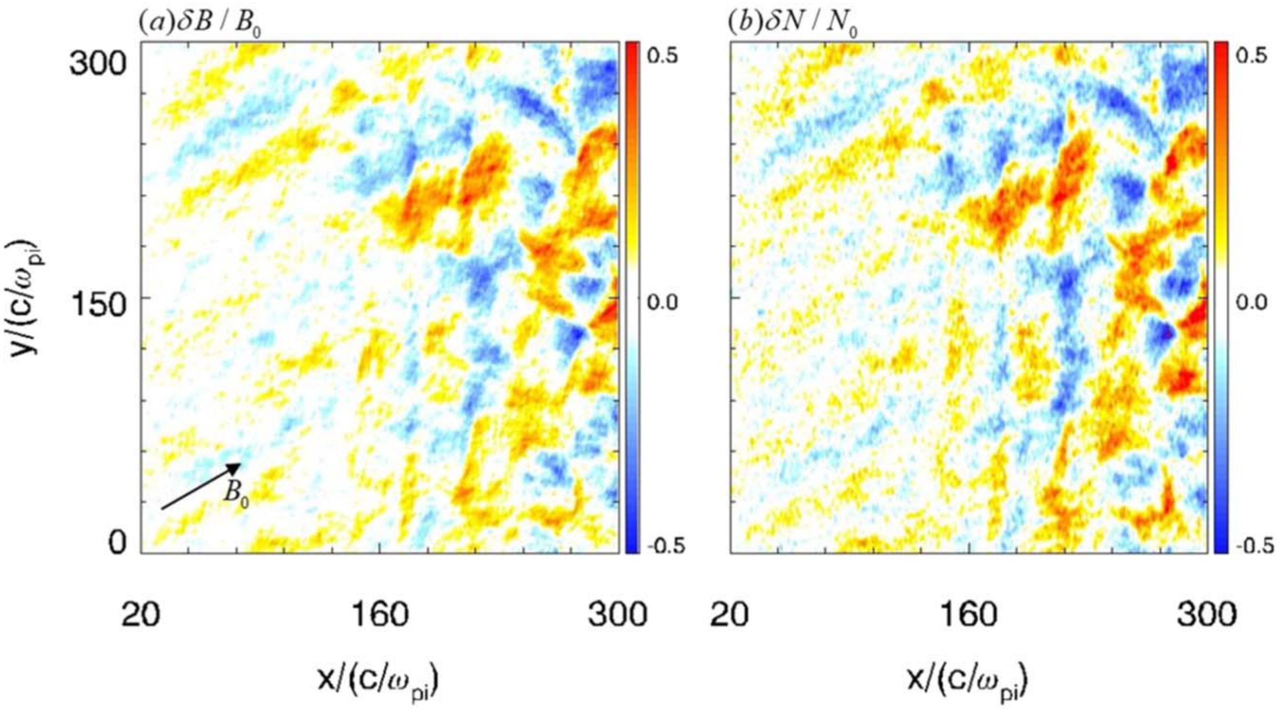

Figure 2. Contour plots of variations of (a) total magnetic field and (b) particle number density at time $\Omega_i t = 160$. The black arrow denotes upstream background magnetic field B_0.

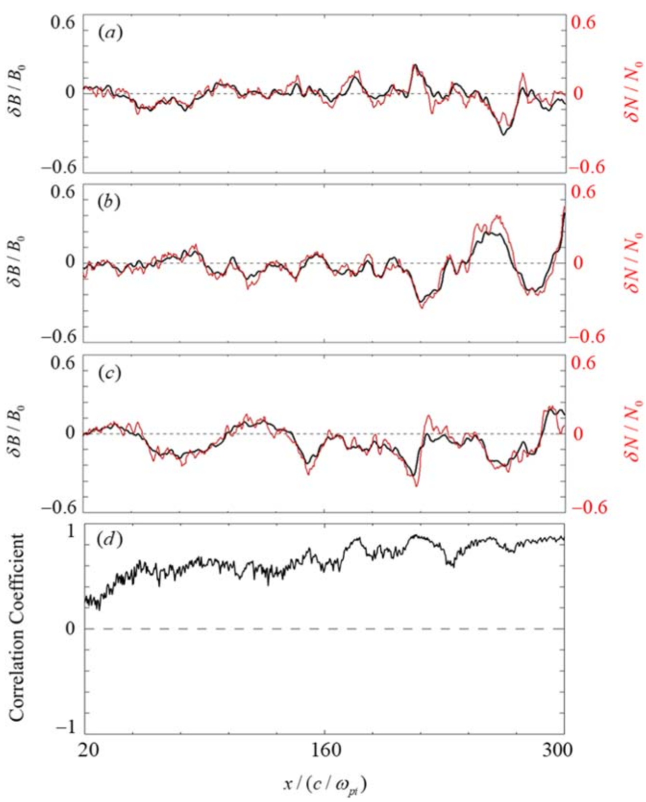

Figure 3. Variations of magnetic fields and particle number density along three cuts parallel to the x direction at $y =$ (a) $50c/\omega_{pi}$, (b) 150 c/ω_{pi}, and (c) $250c/\omega_{pi}$, and (d) their corresponding correlation coefficient calculated in the area as shown in Figure 2.

Figures 3(a)–(c), we can see that along all three cuts the perturbations δB and δN are well correlated and change uniformly. While the amplitude deep in the upstream is larger than that further upstream, which can be explained by more free energy brought by reflected particles when approaching the shock front (Scholer 1993). The correlation coefficient in Figure 3(d) can also confirm that the total magnetic fields are positively correlated with particle number density in the entire upstream area. This means that these waves should be compressive waves, although some unexpected quasi-perpendicular waves coexist in the upstream area.

In Figure 4, we display the variations of three components of magnetic field: (a) $\delta b_x = b_x - \bar{b}_x$, (b) $\delta b_y = b_y - \bar{b}_y$, and (c) b_z, where b_x, b_y, b_z, $\bar{b}_x$, and $\bar{b}_y$ are magnetic field components and the corresponding mean values along the y direction. We divide the upstream region into two parts: further upstream ($20c/\omega_{pi} < x < 150c/\omega_{pi}$) and near upstream ($150c/\omega_{pi} < x < 300c/\omega_{pi}$). Further upstream in Figures 4(a)–(b), we can clearly see that the wave fronts are parallel to the background magnetic field, while in Figure 4(c) there are merely low-amplitude wave fronts almost perpendicular to the background magnetic fields, which implies that the possible quasi-perpendicular propagating waves should be linearly polarized and dominant wave modes in this area. In the near upstream, quasi-perpendicular waves can also be seen in Figure 4(a). Meanwhile, quasi-parallel waves are found in Figures 4(a) and (c), and their wave amplitudes are comparable to that of quasi-perpendicular waves, so that the wave fronts in Figure 4(b) are refracted due to the perturbation δb_y originating from both quasi-perpendicular and quasi-parallel waves besides the above reason that these waves interact with backstreaming particles (Scholer 1993).

For a detailed study of these upstream waves, Figure 5 shows power spectra of the magnetic field perturbations, δb_x, δb_y, and b_z, further upstream, and the black solid lines indicate $k_\perp$ and $k_\parallel$, respectively. In Figures 5(a) and (b), quasi-perpendicular waves can be clearly observed, while in Figure 5(c), there are only quasi-parallel waves with lower

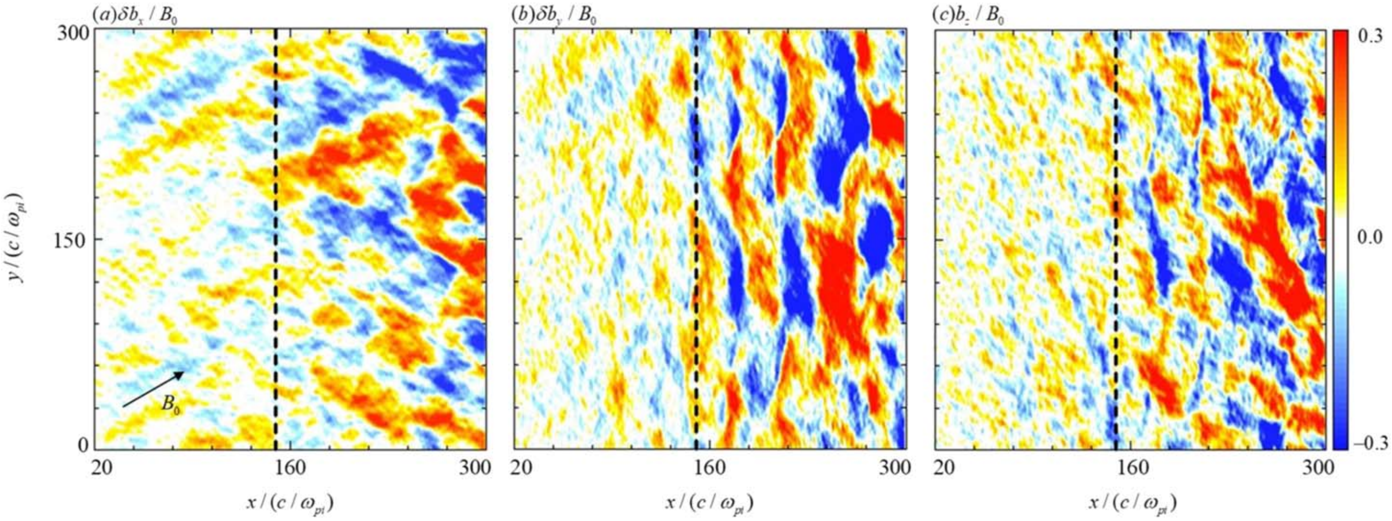

Figure 4. Contour plots of variations of the three magnetic field components: (a) $\delta b_x/B_0$, (b) $\delta b_y/B_0$, and (c) b_z/B_0. The black dashed lines at $x = 150c/\omega_{pi}$ separated the upstream into two areas, and the black arrow denotes the upstream background magnetic field B_0.

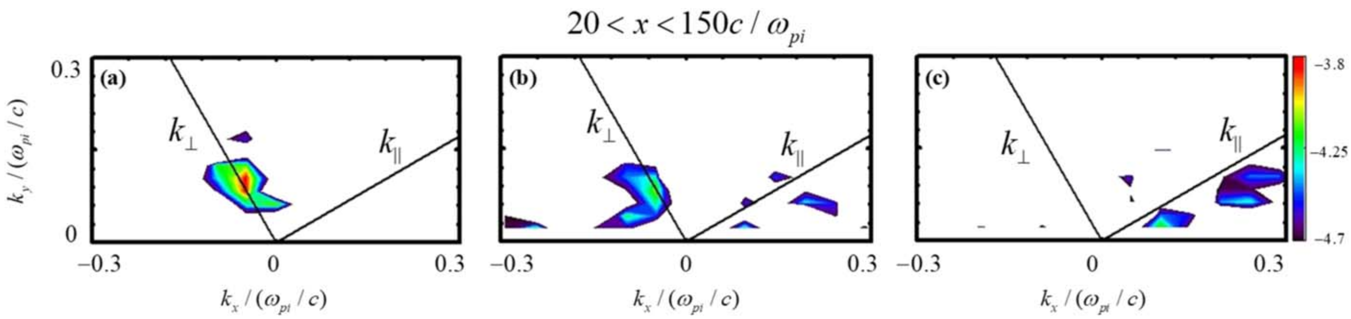

Figure 5. Wave power spectra of the variations in Figure 4 in an area ($20 < x < 150c/\omega_{pi}$, $0 < y < 300c/\omega_{pi}$).

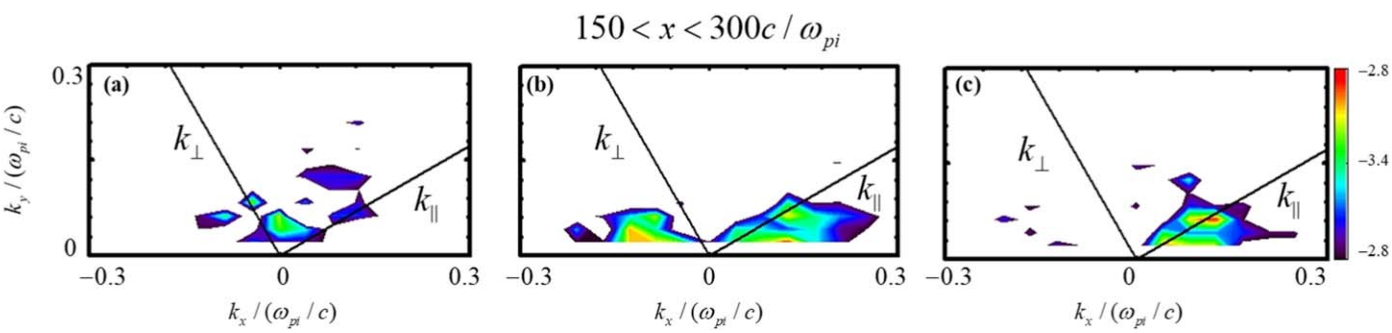

Figure 6. Wave power spectra of the variations in Figure 4 in an area ($150 < x < 300c/\omega_{pi}$,$0 < y < 300c/\omega_{pi}$).

amplitude, which is in agreement with the above suggestion that the quasi-perpendicular waves are linearly polarized and dominant in the further upstream area. Figure 6 shows power spectra of the magnetic field perturbations in the near upstream. Refraction of the quasi-perpendicular waves can be observed when $k_\parallel < 0$ in Figures 6(a)–(b) and quasi-parallel propagating waves in Figures 6(b)–(c) have an amplitude comparable to the former.

We select a group of particles from a region ($10c/\omega_{pi} < x < 30c/\omega_{pi}$, $0c/\omega_{pi} < y < 300c/\omega_{pi}$) to study the ion velocity distributions, so that we can input the velocity distribution functions into a plasma dispersion solver PDRK/BO (Xie & Xiao 2016; Xie 2019) to examine the potential excitation of waves further upstream, and all the analysis results are shown in Figure 7. As the solver, calculations are performed in the background-proton frame, and backward electrons are assumed to generate a return current, which can compensate the original beam current and leads to the formation of a beam-return current system with charge-neutrality and zero-current conditions. The top panel in Figure 7 displays the ion distribution of these selected particles in phase space ($v_\parallel$, $v_\perp$), where $v_\parallel$ and $v_\perp$ denote the ion velocity components in the directions parallel and perpendicular to the upstream background magnetic field. At about $v_\parallel = 4.5V_A$, we can see a cold core corresponding to the incident flow and shell-like components corresponding to the backstreaming particles with higher energy after reflection and subsequent acceleration (Su et al. 2012b; Hao et al. 2016b). The shell-like distribution should result from pitch-angle scattering of

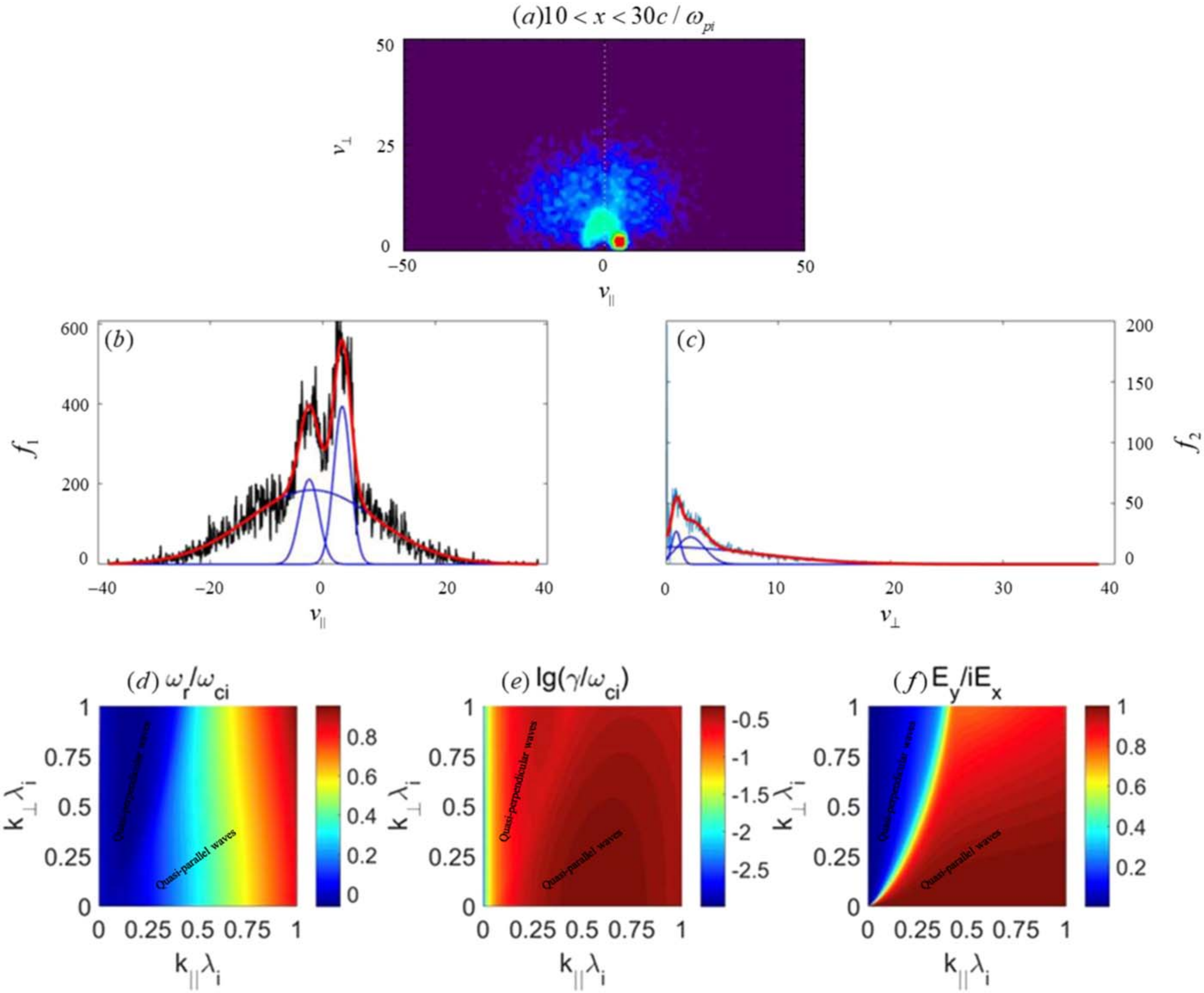

Figure 7. (a) The contour plot of velocity space distribution $f(v_{//}, v_{\perp})$ of particles in the regions $10 < x < 30c/\omega_{pi}$ with all the grid cells in the y direction. ((b) and (c)) The velocity distribution functions $f(v_{\|})$ and $f(v_{\perp})$ denoted by the highly fluctuated solid lines are fitted by Equations (1) and (2) with three Maxwellian distributions indicated with smooth blue lines, and the resulting entire velocity distributions are denoted by the smooth red solid lines. ((d)–(f)) Contour plots of plasma dispersion relations calculated by the linear theory solver PDRK/BO and the fitting parameters in Table 1, including wave frequency ω_r/ω_{ci}, growth rate γ/ω_{ci}, and electric polarization ratios E_y/iE_x in the $k_{\|} - k_{\perp}$ space.

backstreaming particles by upstream waves (Winske & Leroy 1984).

In Figures 7(b) and (c), the ion velocity distributions $f(v_{\|})$ and $f(v_{\perp})$ are fitted to three Maxwellian components,

$$f_1 = f(v_{\|}) = a_1 \cdot e^{-((x-b_1)/c_1)^2} + a_2 \cdot e^{-((x-b_2)/c_2)^2} + a_3 \cdot e^{-((x-b_3)/c_3)^2}, \quad (1)$$

$$f_2 = f(v_{\perp}) = a_1 \cdot e^{-((x-b_1)/c_1)^2} + a_2 \cdot e^{-((x-b_2)/c_2)^2} + a_3 \cdot e^{-(x/c_3)^2}, \quad (2)$$

where a_i, b_i, and c_i ($i = 1, 2, 3$) are fitting parameters, and they are used to calculate dispersion relations as input parameters shown in Table 1. Figure 7(b) shows that, besides the incident flow at about $v_{\|} = 4.5V_A$, there are two beams in the parallel direction, and two perpendicular beams can also be observed at f_2. With the assistance of PDRK/BO, the associated parameters, including wave frequency ω_r/ω_{ci}, growth rate γ/ω_{ci},

Table 1
Fitting Parameters in Equations (1)–(3)

	a_1	b_1	c_1	a_2	b_2	c_2	a_3	b_3	c_3
f_1	211.5	2.4	2.5	184.7	−1.9	16.3	394.3	3.5	2.1
f_2	27.2	0.9	0.6	22.4	2.2	1.8	14.2	0.0	11.4
f_3	609.4	−5.6	10.6	449.7	4.2	4.1	0.0	0.0	0.0

and electric polarization ratios E_y/iE_x, are calculated and displayed in Figures 7(d)–(f), where we can see that two types of waves can be excited by prediction of dispersion analysis of particle distribution from further upstream. The first type is a quasi-parallel fast magnetosonic wave with a right-hand polarization ($E_y/iE_x \sim 1$), a phase velocity close to the Alfvén speed and the largest growth rate. The second type is a highly oblique fast magnetosonic wave with linear polarization

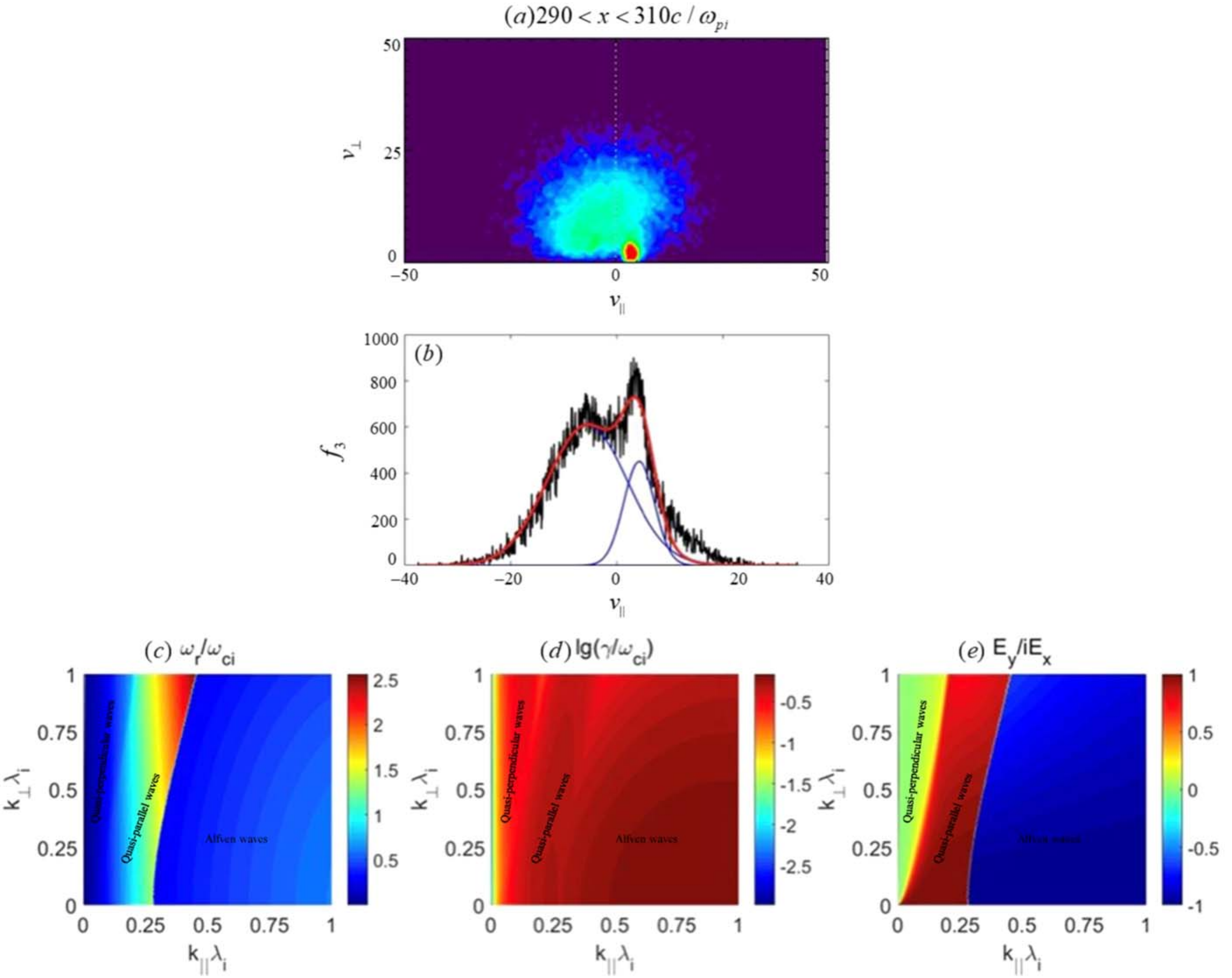

Figure 8. (a) The contour plot of velocity space distribution $f(v_{//}, v_{\perp})$ of particles in the region $290 < x < 310c/\omega_{pi}$ with all the grid cells in the y direction. (b) The velocity distribution function $f(v_{\|})$ denoted by the highly fluctuated solid line is fitted by Equation (3) with two Maxwellian distributions indicated with the smooth blue lines, and the resulting entire velocity distribution are denoted by the smooth red solid line. (c)–(e) Contour plots of plasma dispersion relations calculated by the linear theory solver PDRK/BO and the fitting parameters in Table 1, including frequency ω_r/ω_{ci}, growth rate γ/ω_{ci}, and electric polarization ratios E_y/iE_x in the $k_{\|} - k_{\perp}$ space.

($E_y/iE_x \sim 0$), an almost zero phase velocity ($\omega_r/\omega_{ci} \sim 0$), and a slightly lower growth rate. That the simplified ring beam function used in PDRK/BO cannot provide enough free energy as a shell-like distribution (Sun et al. 2016, 2017) may be the reason for the lower growth rate of highly oblique waves, which are actually dominant wave modes in the further upstream area. Through theoretical studies this distribution has demonstrated that it can indeed drive quasi-perpendicular fast magnetosonic waves (Liu et al. 2011; Min & Liu 2015a, 2015b), quasi-parallel fast magnetosonic waves, and even Alfvén waves (Wu & Yoon 1990).

We perform the same analysis for the near upstream by selecting a group of particles in a region ($290c/\omega_{pi} < x < 310c/\omega_{pi}$, $0c/\omega_{pi} < y < 300c/\omega_{pi}$), and the results are shown in Figure 8. The ion velocity distribution in the near upstream presents a cold core corresponding to the incident flow, and a superthermal population can be found as shown in Figure 8(a). We fit the parallel velocity distribution using the following equation,

$$f_3 = f(v_{\|}) = a_1 \cdot e^{-((x-b_1)/c_1)^2} + a_2 \cdot e^{-((x-b_2)/c_2)^2}. \quad (3)$$

The fitting result also shows a cold beam and a superthermal particle flow (see the associated fitting parameters in Table 1). Based on the fitting parameters, linear theory predicts that this distribution can drive three types of wave modes: (i) quasi-parallel right-hand polarized fast magnetosonic waves ($E_y/iE_x \sim 1$) with a phase velocity $\sim V_A$ and a large growth rate; (2) left-hand Alfvén/ion cyclotron waves ($E_y/iE_x \sim -1$); and (3) highly oblique magnetosonic waves with linear polarization ($E_y/iE_x \sim 0$), an almost zero phase velocity ($\omega_r/\omega_{ci} \sim 0$), and a lower growth rate, as shown in the bottom panels of Figure 8. Remarkably, for the highly oblique waves, their growth rates in the region close to the shock front are also lower compared to other wave modes predicted by linear theory, while the amplitude of these waves is considerable in this upstream area. It can be explained by the quasi-perpendicular waves driven in further upstream and their convection to near upstream by incident plasma due to their almost zero phase velocity, which can become the seed waves and ensure their comparable amplitude in the deep foreshock before the shock front. The Alfvén/ion cyclotron waves predicted by linear theory have not been identified in our simulations due to their similar propagating directions to the fast magnetosonic waves, although in situ observations in terrestrial foreshock also suggest their existence (Blanco-Cano & Schwartz 1997; Eastwood et al. 2003).

4. Conclusions and Discussion

In this paper, we investigate low-frequency upstream waves at a quasi-parallel shock by a 2D hybrid simulation code. We find that in the near upstream the reflected particles form a superthermal population that can provide free energy for several plasma wave modes by prediction of linear theory. Two types of fast magnetosonic waves can be distinctly identified from simulations in this upstream area close to the shock front. They are quasi-parallel propagating, right-hand polarized waves and the waves propagating at a highly oblique angle to the upstream background magnetic field with a linear polarization. Some of these superthermal particles may continue to backstream to further upstream and are scattered by the above excited upstream waves into a shell-like velocity distribution, which can also drive these two types of waves. Meanwhile, in the further upstream area, the quasi-perpendicular waves become the dominant modes. Similarly, the excitation of these waves further upstream is consistent to the dispersion relation calculated by the solver PDRK/BO for linear theory.

Foreshock waves of the terrestrial bow shock have been getting attention for decades to investigate the evolution of the shock front, the associated ion dynamics, and the possible effect on the magnetosphere (Burgess 1989; Schwartz & Burgess 1991; Scholer & Burgess 1992; Scholer 1993; Greenstadt et al. 1995; Burgess 1997; Wang & Lin 2003; Eastwood et al. 2005c; Zhao et al. 2017). The 30 s waves (Fairfield 1969; Hoppe & Russell 1981; Eastwood et al. 2005a, 2005b), 3 s waves (Russell et al. 1971; Le et al. 1992), and 1 Hz (Hoppe et al. 1981, 1982) waves are the well-known wave modes in the foreshock and have been widely studied (Wilson 2016), especially the first one corresponding to the ULF waves excited upstream of the quasi-parallel shock geometry through the interaction of reflected particles and incident flow (Greenstadt et al. 1995; Burgess 1997; Mazelle et al. 2003; Eastwood et al. 2005c). It is likely that the ULF wave modes are a mixture of the quasi-parallel (Eastwood et al. 2004) and quasi-perpendicular fast magnetosonic waves due to their similar wavelengths and comparable amplitude in regions near the shock front or the dominant quasi-perpendicular waves in further upstream areas, and they all can be brought back into the shock front because of their small phase velocity close to zero or Alfvén speed (Otsuka et al. 2019), which had been investigated by global hybrid simulations to some extent (Lin 2003; Lin & Wang 2005; Blanco-Cano et al. 2006, 2009, 2011; Omidi 2007; Kempf et al. 2015; Palmroth et al. 2015; Turc et al. 2018; Jarvinen et al. 2020). The Alfvén waves observed by spacecraft in the terrestrial foreshock may also be excited in our simulated foreshock by the interaction of superthermal particles with incident particles (Blanco-Cano & Schwartz 1997; Eastwood et al. 2003), even though these waves with considerable growth rate have not been identified because of possible mixing of several groups of wave modes. Finally, the same simulations as performed in this paper were applied to study downstream waves at the quasi-parallel shock by Hao et al. (2018), and they found the downstream quasi-perpendicular propagating kinetic slow waves (KSWs) that are suggested to be generated by the mode conversion of the upstream nearly parallel propagating ULF waves (Krauss-Varban & Omidi 1991; Krauss-Varban 1995), while here we believe it is more reasonable that these downstream KSWs may originate from the upstream highly oblique fast magnetosonic waves by mode conversion process in shock front, which shed more light on the formation and components of terrestrial magnetosheath turbulence (Alexandrova 2008; Alexandrova et al. 2008; He et al. 2011, 2012; Zank et al. 2015; Huang et al. 2017).

The work was supported by NSFC grants 41804158, 41531071, 11873018, and 11790302, Key Laboratory of Geospace Environment, University of Science & Technology of China, and Anhui Provincial Natural Science Foundation (1808085QD101). The simulation data will be preserved on a long-term storage system and will be made available upon request to the corresponding author.

ORCID iDs

Yufei Hao https://orcid.org/0000-0001-9578-6250
Quanming Lu https://orcid.org/0000-0003-3041-2682
Dejin Wu https://orcid.org/0000-0003-2418-5508
San Lu https://orcid.org/0000-0003-2248-5072

References

Alexandrova, O. 2008, NPGeo, 15, 95
Alexandrova, O., Lacombe, C., & Mangeney, A. 2008, AnGeo, 26, 3585
Axford, W. I., Leer, E., & Skadron, G. 1977, ICRC (Plovdiv), 15, 132
Bell, A. R. 1978, MNRAS, 182, 147
Blanco-Cano, X., Kajdič, P., Omidi, N., & Russell, C. T. 2011, JGRA, 116, A09101
Blanco-Cano, X., Omidi, N., & Russell, C. T. 2006, JGRA, 111, A10205
Blanco-Cano, X., Omidi, N., & Russell, C. T. 2009, JGRA, 114, A01216
Blanco-Cano, X., & Schwartz, S. J. 1997, AnGeo, 15, 273
Blandford, R. D., & Ostriker, J. P. 1978, ApJL, 221, L29
Burgess, D. 1989, GeoRL, 16, 345
Burgess, D. 1997, AdSpR, 20, 673
Eastwood, J. P., Balogh, A., & Lucek, E. A. 2003, AnGeo, 21, 1457
Eastwood, J. P., Balogh, A., Lucek, E. A., Mazelle, C., & Dandouras, I. 2005a, JGRA, 110, A11219
Eastwood, J. P., Balogh, A., Lucek, E. A., Mazelle, C., & Dandouras, I. 2005b, JGRA, 110, A11220
Eastwood, J. P., Balogh, A., Mazelle, C., Dandouras, I., & Reme, H. 2004, GeoRL, 31, L04804
Eastwood, J. P., Lucek, E. A., Mazelle, C., et al. 2005c, SSRv, 118, 41
Fairfield, D. H. 1969, JGR, 74, 3541
Gedalin, M. 2016a, PhPl, 23, 102904
Gedalin, M. 2016b, JGRA, 121, 10754
Giacalone, J., Burgess, D., Schwartz, S. J., & Ellison, D. C. 1992, GeoRL, 19, 433
Giacalone, J., & Decker, R. 2010, ApJ, 710, 91
Greenstadt, E., Le, G., & Strangeway, R. 1995, AdSpR, 15, 71
Guo, F., & Giacalone, J. 2010, ApJ, 715, 406
Guo, F., & Giacalone, J. 2013, ApJ, 773, 158
Hao, Y., Gao, X., Lu, Q., et al. 2017, JGRA, 122, 6385
Hao, Y., Lembège, B., Lu, Q., & Guo, F. 2016a, JGRA, 121, 2080
Hao, Y., Lu, Q., Gao, X., et al. 2018, ApJ, 861, 57
Hao, Y., Lu, Q., Gao, X., & Wang, S. 2016b, ApJ, 823, 7
He, J. S., Marsch, E., Tu, C., Yao, S., & Tian, H. 2011, ApJ, 731, 85

He, J. S., Tu, C., Marsch, E., & Yao, S. 2012, ApJL, 745, L8
Hoppe, M., & Russell, C. 1981, AdSpR, 1, 327
Hoppe, M. M., Russell, C. T., Eastman, T. E., & Frank, L. A. 1982, JGR, 87, 643
Hoppe, M. M., Russell, C. T., Frank, L. A., Eastman, T. E., & Greenstadt, E. W. 1981, JGR, 86, 4471
Huang, S. Y., Hadid, L. Z., Sahraoui, F., Yuan, Z. G., & Deng, X. H. 2017, ApJL, 836, L10
Jarvinen, R., Alho, M., Kallio, E., & Pulkkinen, T. I. 2020, MNRAS, 491, 4147
Kempf, Y., Pokhotelov, D., Gutynska, O., et al. 2015, JGRA, 120, 3684
Krauss-Varban, D. 1995, AdSpR, 15, 271
Krauss-Varban, D., & Omidi, N. 1991, JGR, 96, 17715
Le, G., Russell, C., Thomsen, M., & Gosling, J. 1992, JGR, 97, 2917
Lembege, B., Giacalone, J., Scholer, M., et al. 2004, SSRv, 110, 161
Lin, Y. 2003, JGRA, 108, 1390
Lin, Y., & Wang, X. Y. 2005, JGRA, 110, A12216
Liu, K., Gary, S. P., & Winske, D. 2011, JGRA, 116, A07212
Liu, T. Z., Hao, Y., Wilson, L. B., III, Turner, D. L., & Zhang, H. 2021, GeoRL, 47, e91184
Liu, Z., Turner, D. L., Angelopoulos, V., & Omidi, N. 2015, GeoRL, 42, 7860
Lu, Q., Hu, Q., & Zank, G. P. 2009, ApJ, 706, 687
Lu, Q., Wang, H., Wang, X., et al. 2020, GeoRL, 47, e85661
Mazelle, C., Meziane, K., LeQuéau, D., et al. 2003, P&SS, 51, 785
Min, K., & Liu, K. 2015a, JGRA, 120, 2739
Min, K., & Liu, K. 2015b, JGRA, 120, 8448
Omidi, N. 2007, in AIP Conf. Ser. 932, Turbulence and Nonlinear Processes in Astrophysical Plasma, ed. D. Shaikh & G. Zank (Melville, NY: AIP), 181
Otsuka, F., Matsukiyo, S., & Hada, T. 2019, HEDP, 33, 100709
Palmroth, M., Archer, M., Vainio, R., et al. 2015, JGRA, 120, 8782
Quest, K. B. 1988, JGR, 93, 9649
Russell, C. T., Childers, D. D., & Coleman, P. J. 1971, JGR, 76, 845
Scholer, M. 1993, JGR, 98, 47
Scholer, M., & Burgess, D. 1992, JGR, 97, 8319
Scholer, M., Fujimoto, M., & Kucharek, H. 1993, JGR, 98, 18971
Schwartz, S. J., & Burgess, D. 1991, GeoRL, 18, 373
Su, Y., Lu, Q., Gao, X., Huang, C., & Wang, S. 2012a, PhPl, 19, 092108
Su, Y., Lu, Q., Huang, C., et al. 2012b, JGRA, 117, A08107
Sun, J., Gao, X., Lu, Q., et al. 2016, PhPl, 23, 022902
Sun, J., Gao, X., Lu, Q., et al. 2017, JGRA, 122, 5377
Turc, L., Ganse, U., Pfau-Kempf, Y., et al. 2018, JGRA, 123, 5476
Wang, X. Y., & Lin, Y. 2003, PhPl, 10, 9
Webb, G. M., Zank, G. P., Ko, C. M., & Donohue, D. J. 1995, ApJ, 453, 178
Wilson, L. B. 2016, in Low Frequency Waves at and Upstream of Collisionless Shocks, ed. A. Keiling et al. (New York: Wiley), 291
Wilson, L. B., III, Koval, A., Sibeck, D. G., et al. 2013, JGRA, 118, 957
Winske, D., & Leroy, M. M. 1984, JGR, 89, 2673
Wu, C. S., & Yoon, P. H. 1990, JGR, 95, 10273
Xie, H., & Xiao, Y. 2016, PlST, 18, 97
Xie, H. S. 2019, CoPhC, 244, 343
Yang, Z. W., Lu, Q. M., Lembège, B., & Wang, S. 2009a, JGRA, 114, A03111
Yang, Z. W., Lu, Q. M., & Wang, S. 2009b, PhPl, 16, 124502
Zank, G. P., Hunana, P., Mostafavi, P., et al. 2015, ApJ, 814, 137
Zank, G. P., Pauls, H. L., Cairns, I. H., & Webb, G. M. 1996, JGR, 101, 457
Zhao, L. L., Zhang, H., & Zong, Q. G. 2017, GeoRL, 44, 5283